Chapter 8.5 Airfoil and Wing Theory and Forces on Lifting Bodies

The results for the drag and lift for a circular cylinder with circulation (uniform stream + diploe + vortex) showed according to the Kutta-Joukowski theorem that the drag = 0 (d'Alembert paradox) and the lift = $\rho U \Gamma$ (for clockwise vortex rotation), which can be generalized using complex variables and conformal mapping for any arbitrary non-circular cross sectional shape such as, in particular, airfoil sections with sharp trailing edges.

However, the value of the circulation is not unique, and must be prescribed, which is accomplished for airfoils based on physics, i.e., the Kutta condition: in flow over a two-dimensional body with a sharp trailing edge, there develops a circulation of magnitude just sufficient to move the stagnation point to the training edge.
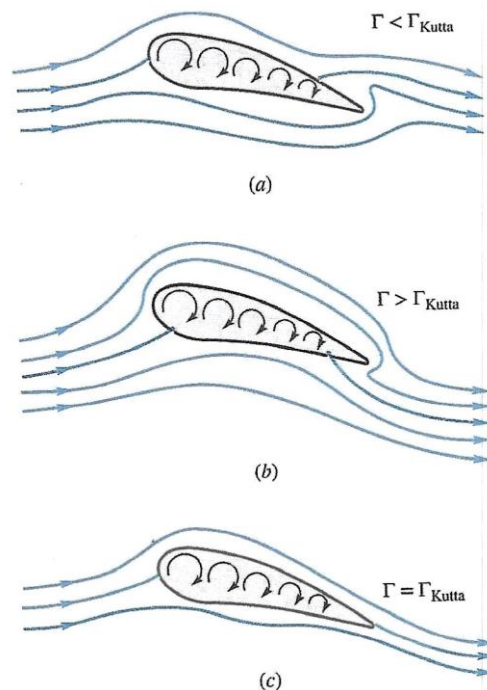

Fig. 8.22 The Kutta condition properly simulates the flow about an airfoil; (a) too little circulation, stagnation point on rear upper surface; (b) too much, stagnation point on rear lower surface; (c) just right, Kutta condition requires smooth flow at trailing edge.

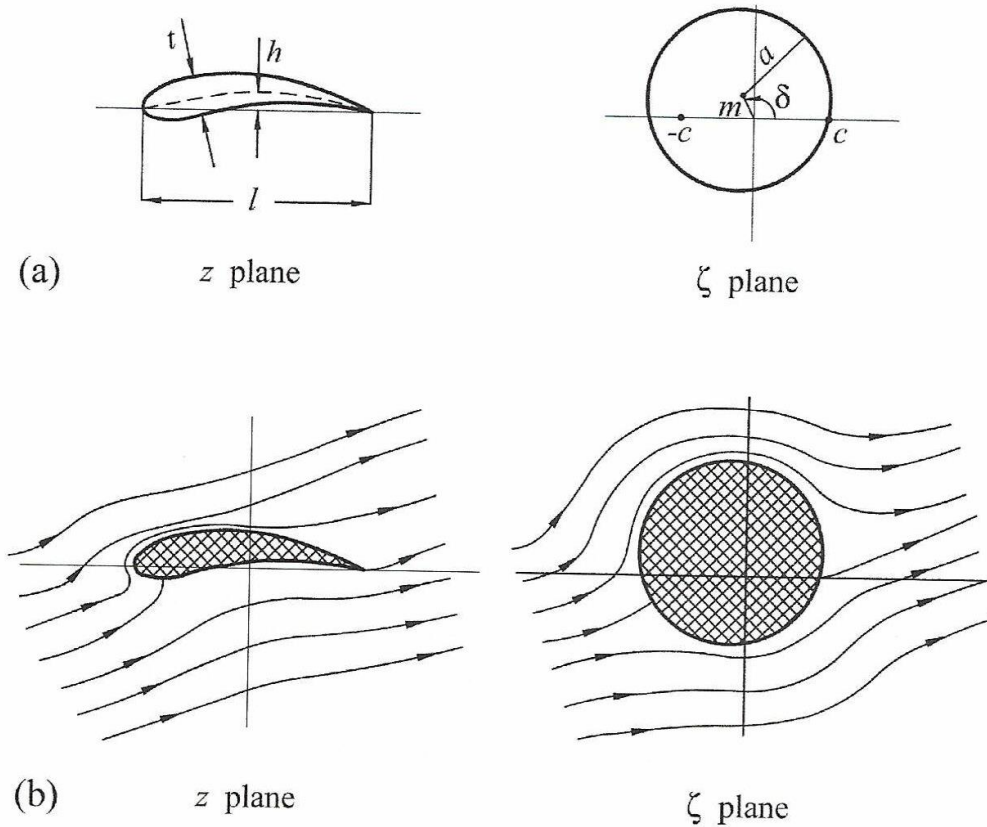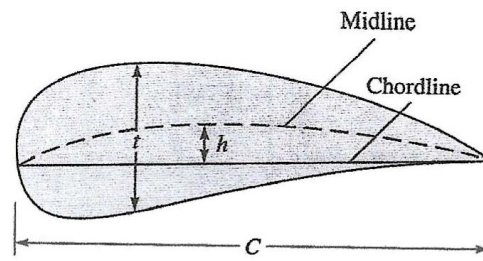# Potential theory for thick[1] cambered airfoils, e.g., the Joukowski airfoil:

(a)   z plane   ζ plane

(b)   z plane   ζ plane

FIGURE 4.18   The Joukowski airfoil: (a) the mapping planes and (b) uniform flow past the airfoil.

---

[1] Thin airfoil theory neglects thickness and distributes vortices of strength $\gamma(x)$ along the camber line with their strength determined such that the flow is tangent to the camber line, which automatically satisfies the Kutta condition.

predicts circulation

$$\Gamma_{\text{Kutta}} = \pi C U_\infty \left(1 + 0.77 \frac{t}{C} \right) \sin(\alpha + \beta)$$

[where $\beta = \tan^{-1}(2h/C)$ and h is the maximum camber, i.e., deviation of the airfoil midline from its chord line C] and lift coefficient

$$C_L = \frac{\rho U_\infty \Gamma b}{\frac{1}{2}\rho U_\infty^2 bC} = 2\pi \left(1 + 0.77 \frac{t}{C} \right) \sin(\alpha + \beta)$$
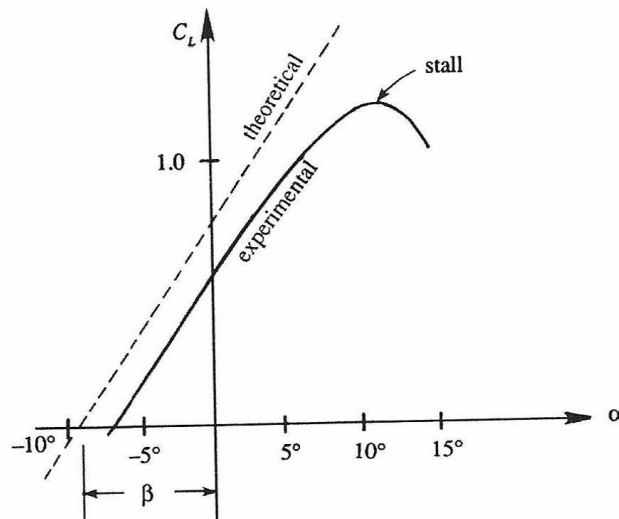

FIGURE 14.18 Comparison of theoretical and experimental lift coefficients for a cambered Zhukhovsky airfoil. The lift curve slopes match well and boundary-layer thicknesses may account for the offset between theoretical and measured curves. The most important difference is that the real airfoil stalls while the ideal one does not.

However, the thickness effect is not validated by experiments (Fig. 8.23) due to boundary layer growth on the upper surface such that it is usually neglected, i.e.,

$$\boxed{C_L \approx 2\pi \sin(\alpha + \beta)}$$

For α = 0 cambered airfoils have finite lift and zero lift at $\alpha_{ZL} = -\beta$, which is over predicted by 1° or more as shown in Table 8.3. NACA series XX indicates t/C in % and other digits refer to camber and other details.
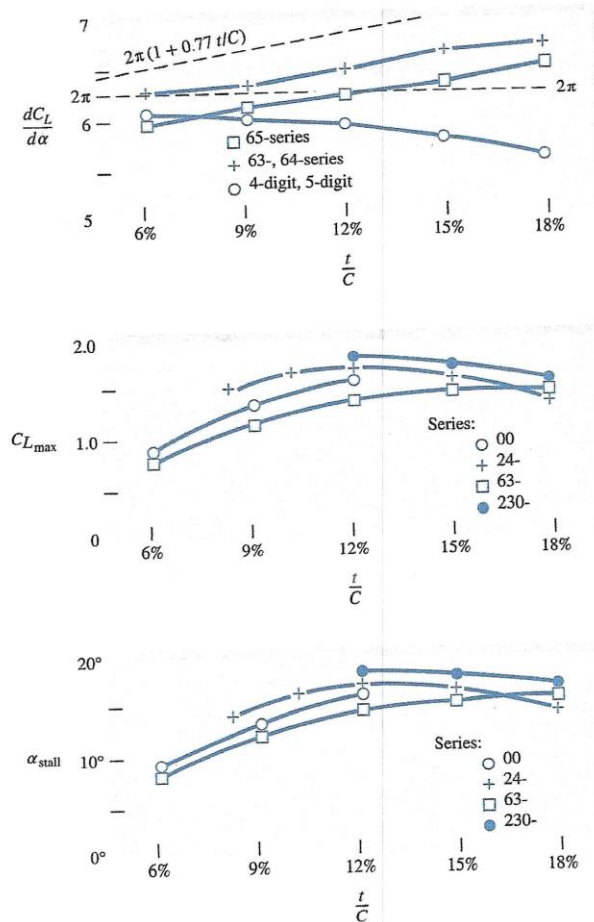

Fig. 8.23 Lift characteristics of smooth NACA airfoils as a function of thickness ratio, for infinite aspect ratio. *(From Ref. 12.)*

Table 8.3 Zero-Lift Angle of NACA Airfoils

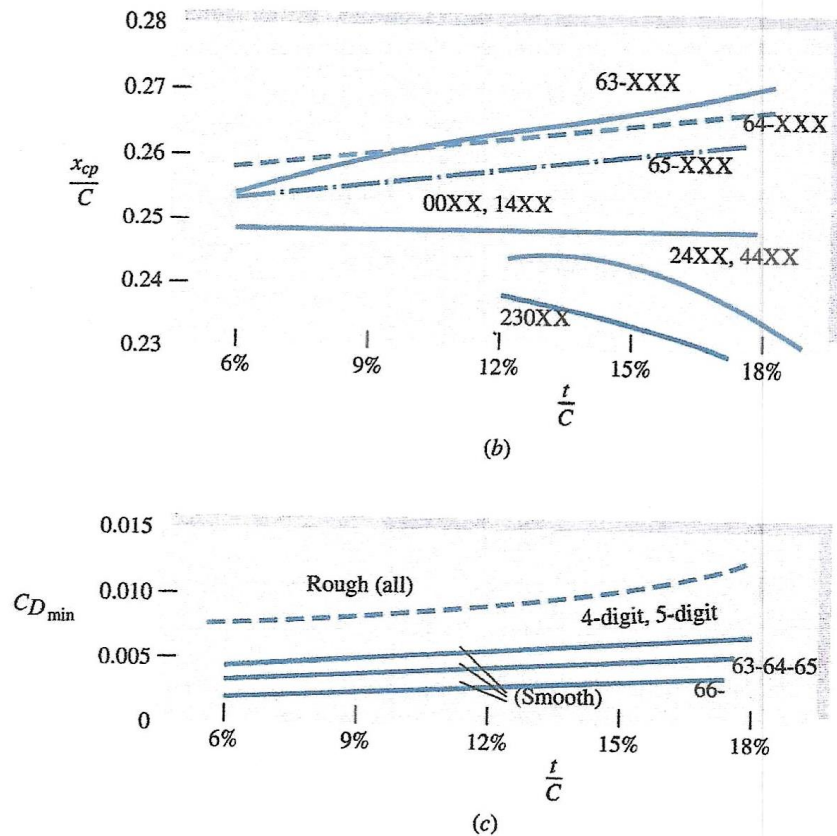| Airfoil series	Camber h/C, %	Measured α_{ZL}, deg	Theory—β, deg
24XX	2.0	–2.1	–2.3
44XX	4.0	–4.0	–4.6
230XX	1.8	–1.3	–2.1
63-2XX	2.2	–1.8	–2.5
63-4XX	4.4	–3.1	–5.0
64-1XX	1.1	–0.8	–1.2

Fig. 8.24 Characteristics of NACA airfoils: (a) typical thick cambered airfoil; (b) center-of-pressure data; and (c) minimum drag coefficient.

Fig. 8.24 shows that the location of the center of pressure x_{CP} is within $.02C$ of $x/C = .25$: standard camber foils lie slightly forward, low drag foils slightly aft, and symmetric foils are at $x/C = .25$.

C_{Dmin} for smooth NACA airfoils have less drag than that for a smooth turbulent flat plate, especially low drag 60 series, whereas with standard surface roughness all foils have the same minimum drag, which is roughly 30% greater than that for the smooth turbulent flat plates.

The aspect ratio for wings of finite span is:

$$\text{AR} = \frac{b^2}{A_p} = \frac{b}{\bar{C}}$$

Where b is the span length from tip to tip, A_p is the planform area as seen from above, and $\bar{C}$ is the average chord length. The lift generation pressure difference creates tip vortices, which extend far downstream. The Helmholtz Theorem #1 is based on the definition of vorticity:

$$\underline{\omega} = \nabla \times \underline{V}$$

$$\nabla \cdot \underline{\omega} = \nabla \cdot (\nabla \times \underline{V}) = 0$$

A vortex line cannot end in the fluid. It must form a closed path (smoke ring), end at a boundary, solid or free surface, or go to infinity.
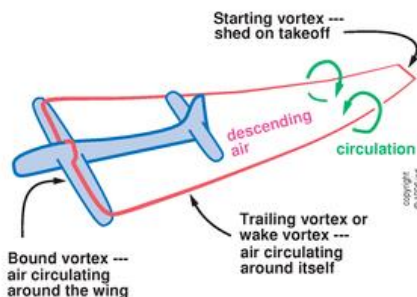
A finite aspect ratio wing can be modeled by a bound vortex system with effective circulation $\Gamma(y)$ which is maximum at the center plane and zero at the tips. Prandtl (1918) further simplified the wing vortex system by the single lifting line and a continuous sheet of semi-infinite trailing vortices of strength $\gamma(y) = d\Gamma/dy$.
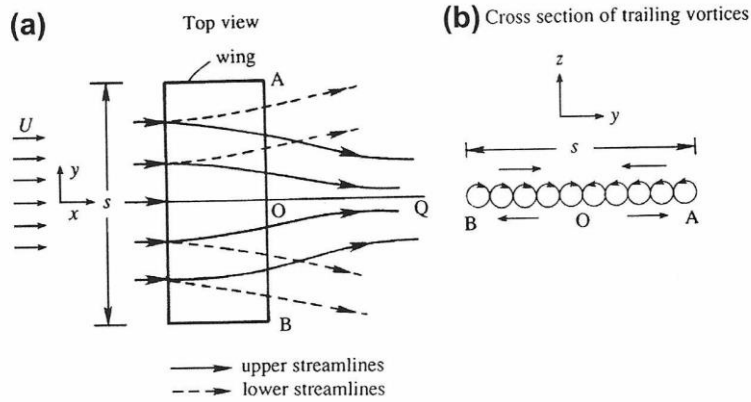
FIGURE 14.20 Flow over a wing of finite span: (a) top view of streamline patterns on the upper and lower surfaces of the wing; and (b) cross-section of trailing vortices behind the wing. The trailing vortices change sign at O, the center of the wing.
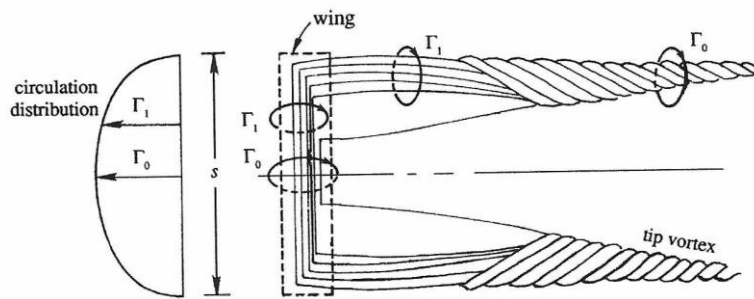

FIGURE 14.21 Rolling up of trailing vortices to form tip vortices. The mutual interaction of the trailing vortices eventually produces two counter-rotating wing-tip vortices having the same circulation as that bound to the center of the main wing.
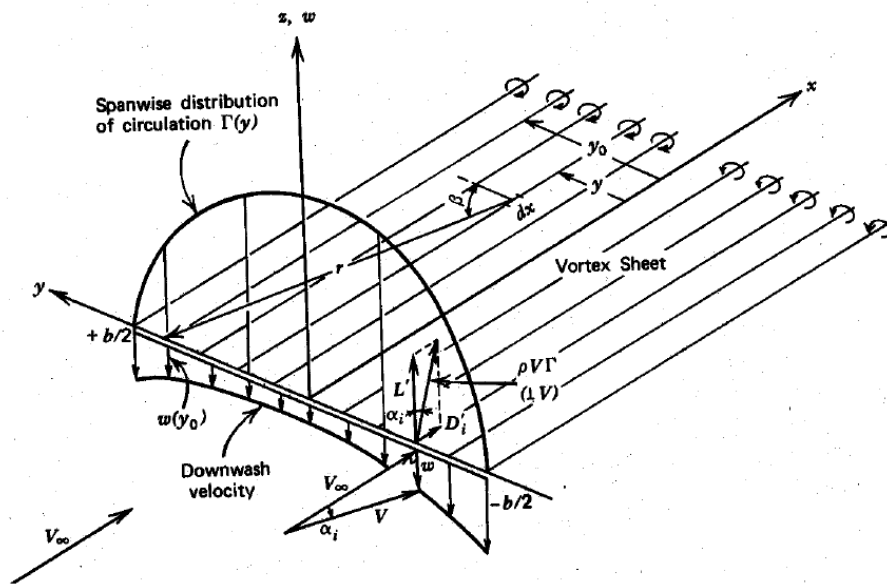

Figure 5: Summary of Key Elements of Lifting Line Theory

Each element of the trailing vortex sheet $\gamma(\eta)d\eta$ induces a downwash, i.e., downward velocity dw(y), which is derived from the Biot-Savart Law that describes the velocity induced at a point in space by a vortex filament:

$$\mathbf{u}(\mathbf{x}, t) = \int_{vortex} d\mathbf{u} \cong \frac{\Gamma}{4\pi} \int_{vortex} \mathbf{e}_\omega \times \frac{(\mathbf{x} - \mathbf{x}')}{|\mathbf{x} - \mathbf{x}'|^3} dl,$$
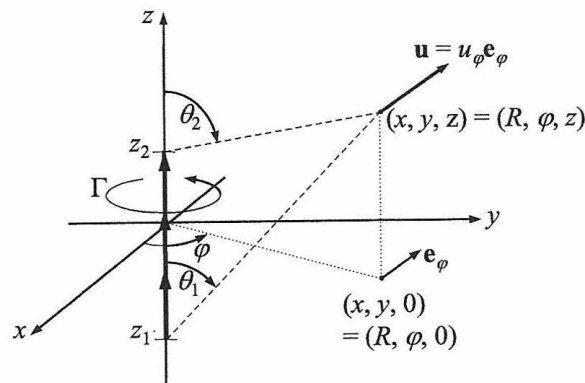

FIGURE 5.10   Geometry for determination of the induced velocity **u** from a straight ideal vortex segment with strength Γ that lies along the z-axis between $z = z_1$ and $z = z_2$. Here the induced velocity will be in the $\mathbf{e}_\varphi$ direction and will depend on the polar angles θ_1 and θ_2.

For a straight semi-infinite trailing vortex filament that leaves the wing at y with strength $\gamma(y)$ and remains horizontal the Biot-Savarat Law simplifies as:

$$dw(y) = \frac{\gamma(\eta) \, d\eta}{4\pi (y - \eta)}$$

Note 4π vs. 2π in denominator is because the trailing vortex system extends from 0 to $+\infty$ not $-\infty$ to $+\infty$.

The total downwash is

$$w(y) = \frac{1}{4\pi} \int_{-(1/2)b}^{(1/2)b} \frac{\gamma(\eta)\, d\eta}{y - \eta}$$

The effective angle attack including the effect of the downwash reduces the geometric angle of attack

$$\alpha_{\text{eff}} = \alpha - \alpha_i \qquad \alpha_i = \tan^{-1} \frac{w}{U_\infty} \approx \frac{w}{U_\infty}$$

Note that $w \ll U_\infty$. $\Gamma(y)$ is assumed equal to that of a two-dimensional wing of the same shape and effective angle of attack such that based on thin airfoil theory

$$C_L = \frac{\rho U_\infty \Gamma b}{\frac{1}{2}\rho U_\infty^2 bC} \approx 2\pi\alpha_{\text{eff}}$$

$$\Gamma \approx \pi C U_\infty \alpha_{\text{eff}}$$

Combining w(y) and $\Gamma \approx \pi C U_\infty \alpha_{\text{eff}}$ results in Prandtl's lifting-line theory for a finite span wing

$$\Gamma(y) = \pi C(y) U_\infty \left[\alpha(y) - \frac{1}{4\pi U_\infty} \int_{-(1/2)b}^{(1/2)b} \frac{(d\Gamma/d\eta)\, d\eta}{y - \eta} \right]$$

Which is an integral-differential equation for $\Gamma(y)$ subject to $\Gamma(b/2) = \Gamma(-b/2) = 0$ with solution providing the wing lift and induced drag:

$$L = \rho U_\infty \int_{-(1/2)b}^{(1/2)b} \Gamma(y)\, dy \quad D_i = \rho U_\infty \int_{-(1/2)b}^{(1/2)b} \Gamma(y)\alpha_i(y)\, dy$$

The induced drag is because the downwash causes the lift to have an angle α_i such that

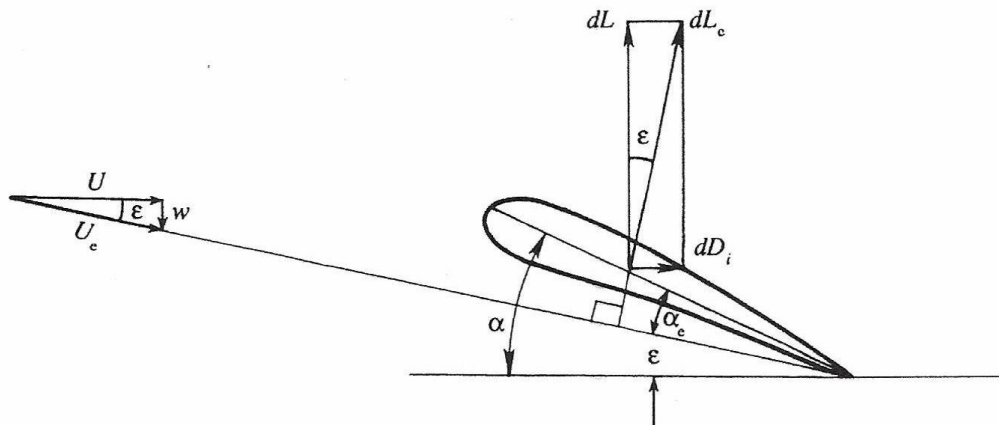$$dDi = dL \sin \alpha_i \approx dL\alpha_i.$$

FIGURE 14.24   Lift and lift-induced drag on a wing element dy in the presence of a downwash velocity w. The downwash velocity locally lowers the angle of attack of the free stream and rotates the lift vector backward to produce the lift-induced drag.

$$\tan(\varepsilon = \alpha_i) = \frac{w}{U_\infty}, \text{ i.e., } \alpha_i \approx \frac{w}{U_\infty}$$

C(y) and α(y) are arbitrary, which requires, advanced methods, but for untwisted elliptical planforms

$$C(y) = C_0 \left[1 - \left(\frac{2y}{b}\right)^2\right]^{1/2} \quad A_p = \int_{-(1/2)b}^{(1/2)b} C\, dy = \frac{1}{4}\pi b C_0 \quad AR = \frac{4b}{\pi C_0}$$

With Γ(y) solution

$$\Gamma(y) = \Gamma_0 \left[1 - \left(\frac{2y}{b}\right)^2\right]^{1/2} \quad \Gamma_0 = \frac{\pi C_0 U_\infty \alpha}{1 + 2/AR}$$

And

$$L = \tfrac{1}{4}\pi^2 b C_0 \rho U_\infty^2 \alpha / (1 + 2/AR)$$

$$C_L = \frac{2\pi\alpha}{1 + 2/AR}$$

Which can be generalized for a thick cambered finite wing of approximately elliptical planform

$$\boxed{C_L = \frac{2\pi \sin(\alpha + \beta)}{1 + 2/AR} = \frac{2L}{\rho U_\infty^2 A_p}}$$

$$C_L = \frac{2\pi(\alpha + \beta)}{1 + 2/AR} = 2\pi\alpha_e$$

$$w(y) = \frac{2U_\infty \alpha}{2 + AR} = \text{const} \quad C_{Di} = C_L \frac{w}{U_\infty} = \frac{C_L^2}{\pi AR}$$

$$\alpha_e = \alpha - \alpha_i = \alpha - \frac{w}{U_\infty} = \alpha - \frac{C_L}{\pi AR}$$
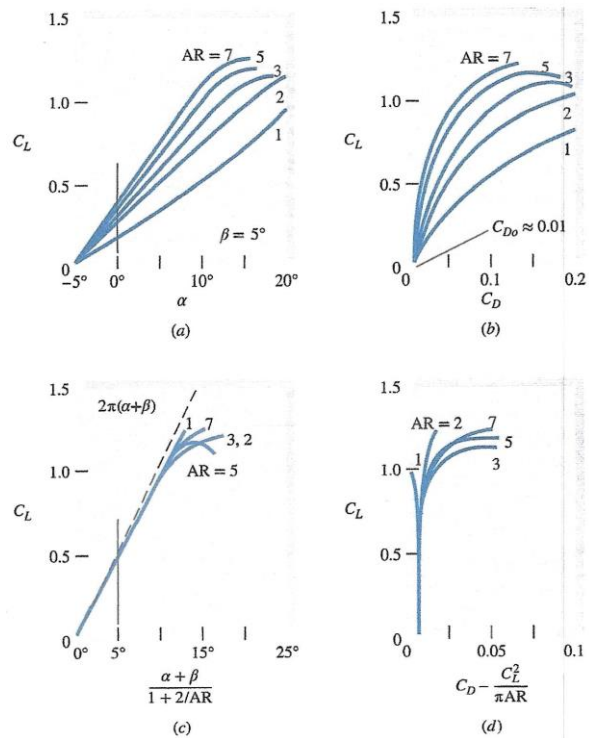
Fig. 8.26 Comparison of theory and experiment for a finite wing: (a) measured lift [14]; (b) measured drag polar [14]; (c) lift reduced to infinite aspect ratio; (d) drag polar reduced to infinite aspect ratio.
Source: Prandtl, L. Applications of Modern Hydrodynamics to Aeronautics. NACA Rep. 116. NASA, 1921.

Fig 8.26 compares theory vs. nonelliptical cambered wings. The stall angle and drag increases and the lift slope decreases as aspect ratio decreases.

Fig. 8.26c shows C_L vs. α_e, which should collapse to an infinite wing, i.e., AR = ∞ and do so except near stall. Their common slope $dC_L/d\alpha_e$ is about 10% less than the theoretical value $2\pi(\alpha + \beta)$, which is consistent with the 2D foil thickness and camber effects, as per Fig. 8.23.

Fig. 8.26d shows C_L vs. C_D-C_{Di} and again except near stall the data collapses onto a single curve of nearly constant AR = ∞ drag C_{D0} = .01, as per Fig. 8.24c.

Conclusion: finite wing lifting line theory is useful for design.
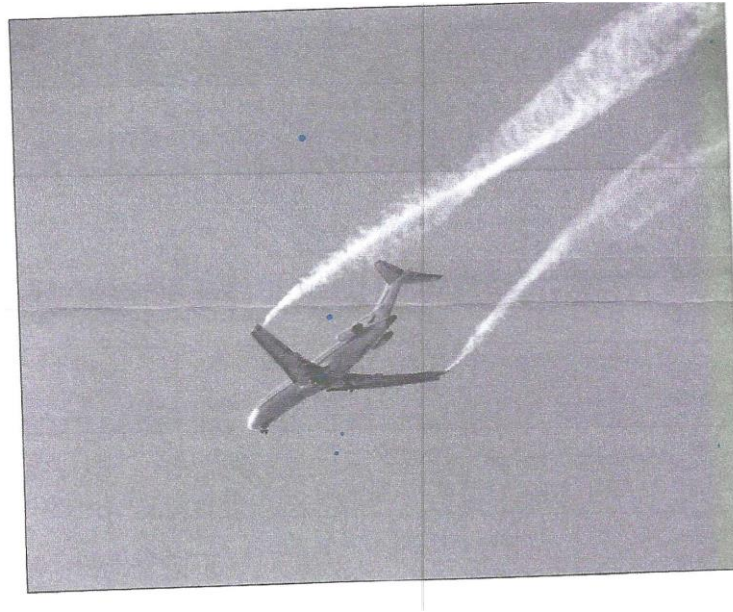
Aircraft Trailing Vortices

Fig. 8.27 Wingtip vortices from a smoke-visualization test of a Boeing 737. Vortices from large airplanes can be extremely dangerous to any following aircraft, especially small planes. This test was part of a research effort to alleviate these swirling wakes. *(NASA)*

Airplane wing tip vortices are long, strong, and lingering, which present a danger to following airplanes by inducing drastic rolling moments, which governs the separation distance between planes at takeoff and governs airport capacity.

Decay of Wake Vortices of Large Aircraft

Turgut Sarpkaya[*]
U.S. Naval Postgraduate School, Monterey, California 93943

A brief summary of previous works is followed by an in-depth analysis of velocities, circulations, and decay histories of a number of trailing vortices generated by large aircraft during field tests in Memphis, Tennessee. The results suggest that the decay of trailing vortices is governed by the mutual straining of vortices; intermittent exchange of mass, momentum, and vorticity across the core boundary; rotational damping and restructuring of turbulence in the core; stretching of large turbulent structures, turbulent diffusion, and the interaction of oppositely signed vorticity in the overlapping regions of the vortex pair; and the draining of vorticity from the Kelvin oval.

Forces on Lifting Bodies

Forces on lifting bodies, such as airfoils, hydrofoils and vanes, are intended to have maximum lift and low drag. Design practices, as per bird wings, are thin (t/c ≤ 0.24) with round leading and sharp trailing edges.
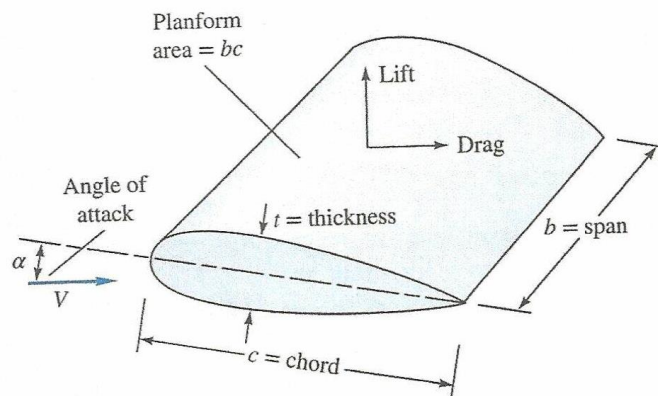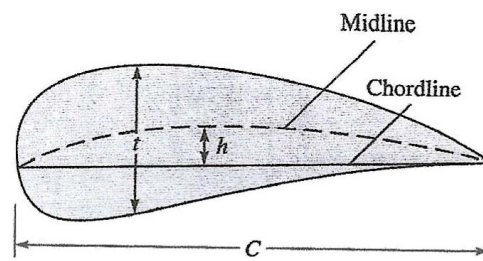

Fig. 7.22 Definition sketch for a lifting vane.

Usually foils/vanes are not symmetric with respect to their chord lines but cambered h=h(c) for optimum design: the camber line is the line midway between the upper and lower surfaces.

Angle of attack α = angle between free stream and chord line. Lift and drag are non-dimensional using planform area A_p= bc or for tapered wings $A_p = \int c\,db$

Lift coefficient:

$$C_L = \frac{L}{\frac{1}{2}\rho V^2 A_p}$$

Drag coefficient:

$$C_D = \frac{D}{\frac{1}{2}\rho V^2 A_p}$$

For low-speed/incompressible flow and constant roughness:

$$C_L = f(\alpha, \mathrm{Re}_c) \quad \text{or} \quad C_D = f(\alpha, \mathrm{Re}_c)$$

The rounded leading edge inhibits separation, whereas the sharp trailing edge is related to lift and the Kutta condition for potential flow.

Fig. 7.23 Transient stages in the development of lift: (a) start-up: rear stagnation point on the upper surface: no lift; (b) sharp trailing edge induces separation, and a starting vortex forms: slight lift; (c) starting vortex is shed; and streamlines flow smoothly from trailing edge: lift is now 80 percent developed; (d) starting vortex now shed far behind, trailing edge now very smooth: lift fully developed.
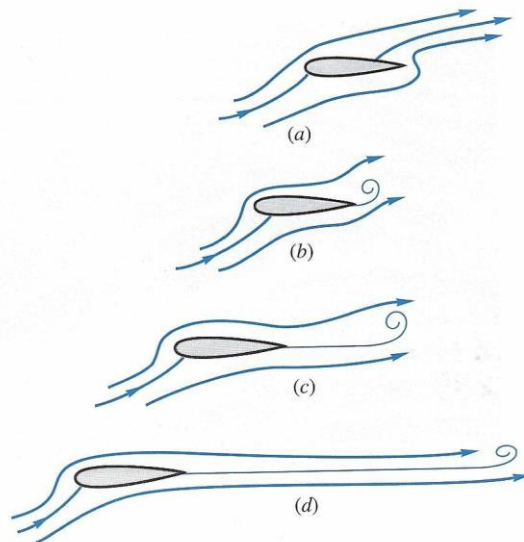
For small α, near the trailing edge the pressure gradient is adverse but weak such that the separation is minimal, and the drag and lift are optimal; however, as α increases the separation increases until at about α = 15 – 20 deg for which the separation is massive and the airfoil stalls, i.e., the lift drops, and the drag increases such that flight is no longer possible.
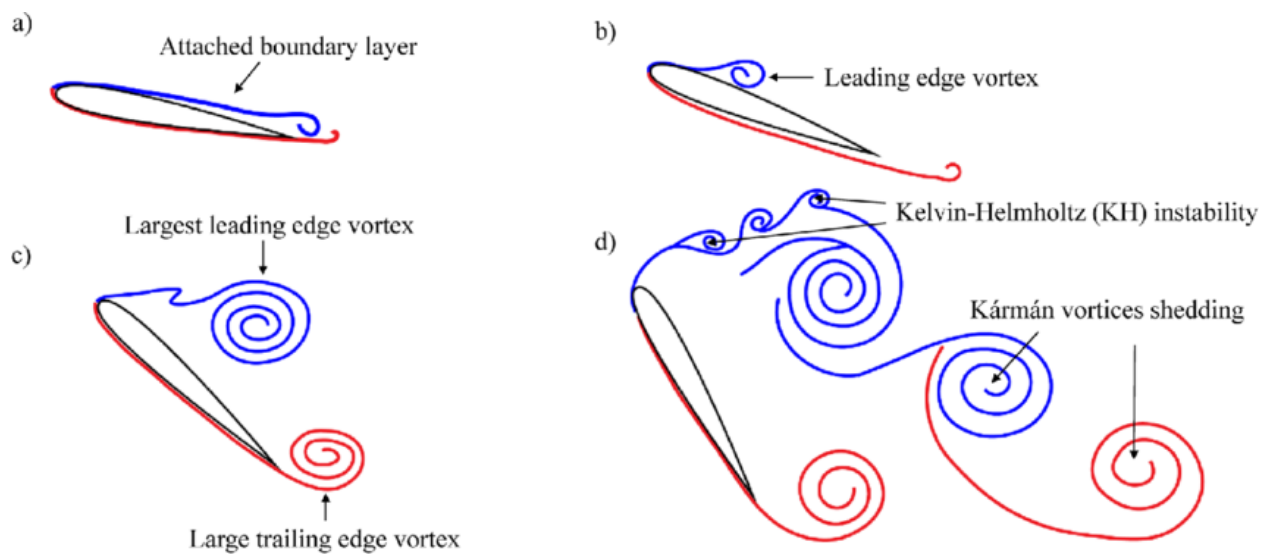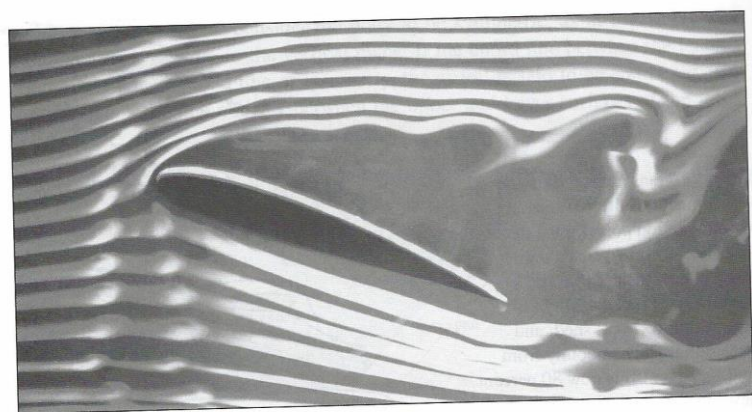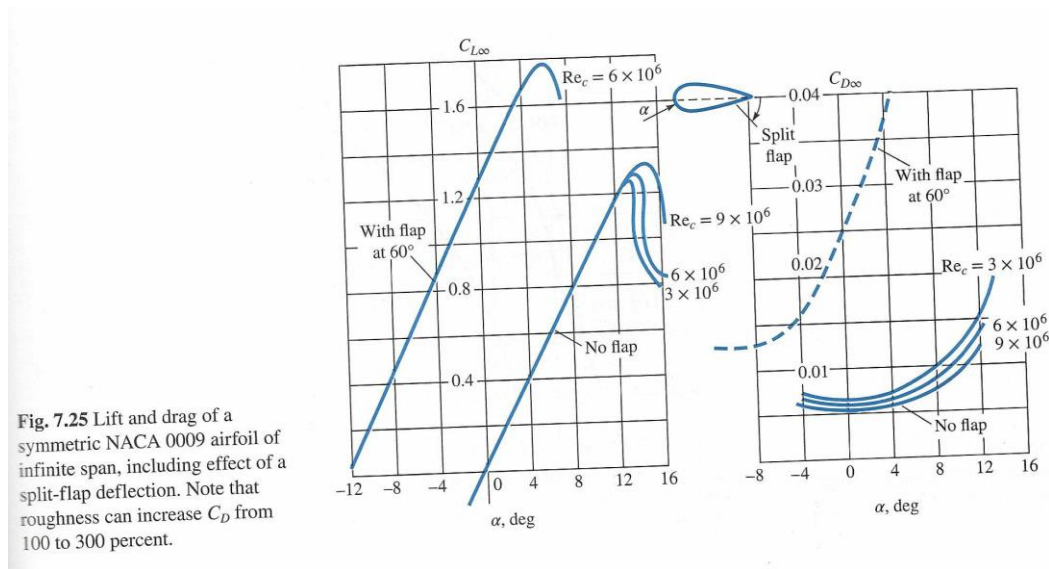

Fig. 7.24 At high angle of attack, smoke flow visualization shows stalled flow on the upper surface of a lifting vane. (*Gary S. Settles & Jason Listak/Science Source*)

[7]For some airfoils the bubble leaps, not creeps, forward, and stall occurs rapidly and dangerously.

Fig. 7.25 Lift and drag of a symmetric NACA 0009 airfoil of infinite span, including effect of a split-flap deflection. Note that roughness can increase C_D from 100 to 300 percent.

Based on thick airfoil theory:

$$C_{L,\text{theory}} \approx 2\pi \sin\left(\alpha + \frac{2h}{c}\right)$$

Fig. 7.25 shows the lift and drag on a NACA symmetric $t/C = 9\%$ airfoil.

Without a flap $C_L = 0$ at $\alpha = 0$. Up to 12 deg the lift increases linearly with slope .11 per deg or 2π per radian, as per airfoil theory.

The drag is as low as .005, which is less than both sides of a turbulent flat plate. However, roughness/paint doubles the drag. Increasing Reynolds number increases the maximum lift and stall angle and reduces the drag.

Flaps are used to increase the lift/camber during takeoff and landing, which changes the zero-lift point to $\alpha = -12$ deg. The drag is increased but the extra power is cost effective as it reduces the takeoff and landing distance.
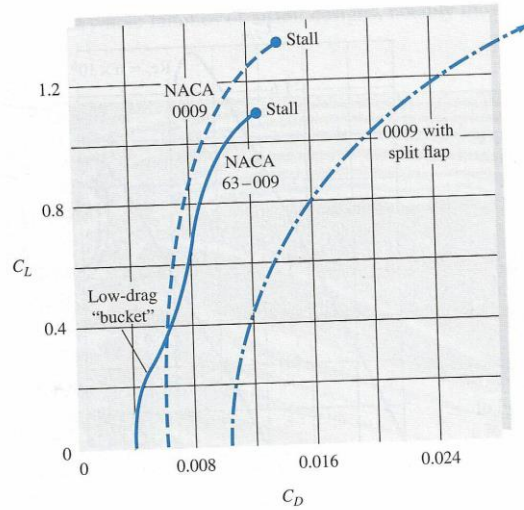
Fig. 7.26 Lift–drag polar plot for standard (0009) and a laminar flow (63-009) NACA airfoil.

Fig. 7.26 lift-drag polar plot compares NACA 0009 and laminar flow NACA 63-009 airfoils (same thickness). The laminar flow foil has a low-drag bucket at small angles but suffers lower stall angle and lower maximum lift. The drag is 30% reduced in the bucket, but the bucket disappears with roughness.

The effects of aspect ratio correlate with the AR:

$$\mathrm{AR} = \frac{b^2}{A_p} = \frac{b}{\bar{c}}$$

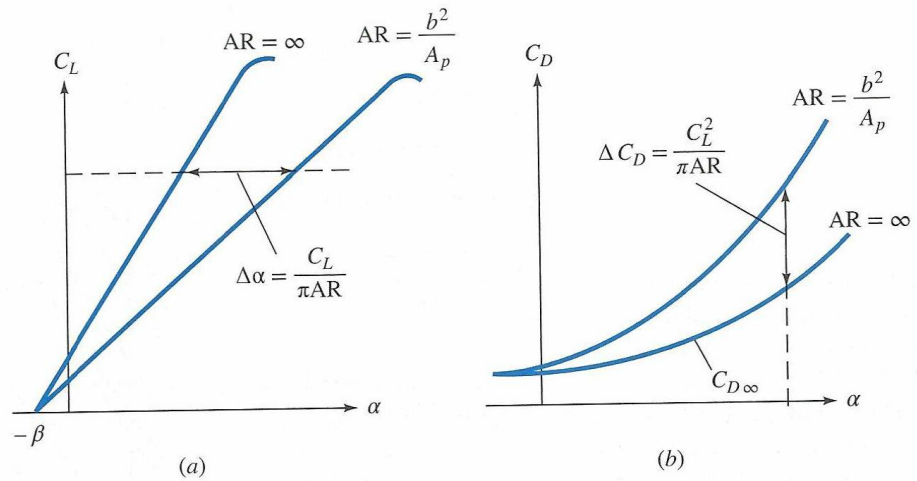Where $\bar{c}$ is the average chord length.

Fig. 7.27 Effect of finite aspect ratio on lift and drag of an airfoil: (*a*) effective angle increase; (*b*) induced drag increase.

Fig. 7.27 shows that finite AR reduces the lift curve slope, but the zero-lift angle is the same; and the drag increases, but the zero-lift drag is the same. Decreasing AR increases the effective angle of attack since α_i, i.e., $\Delta\alpha \approx \dfrac{C_L}{\pi\text{AR}}$ is reduced. Recall

$$C_L \approx \frac{2\pi \sin(\alpha + 2h/c)}{1 + 2/\text{AR}}$$

The associated drag increase is $\Delta C_D \approx C_L \sin \Delta\alpha \approx C_L \Delta\alpha$, or

$$C_D \approx C_{D\infty} + \frac{C_L^2}{\pi\text{AR}}$$

where $C_{D\infty}$ is the drag of the infinite-span airfoil, as sketched in Fig. 7.25.

The stall speed is defined as the speed at maximum lift, which supports the weight:

$$L = W = C_{L,\max}(\tfrac{1}{2}\rho V_s^2 A_p)$$

$$V_s = \left(\frac{2W}{C_{L,\max}\rho A_p}\right)^{1/2}$$

Stall speeds vary between $60 - 200$ ft/s depending on $C_{L\max}$ and the weight. Pilots must hold the speed $>$ than about $1.2V_S$ to avoid stall instabilties.

The split flap (Fig. 7.25) is one of many devices to secure high lift at low speeds. Fig. 7.28a shows additional devices along with their C_L vs. α performance shown in Fig.7.28b.

The double-slotted flap achieves $C_{L,\max} \approx 3.4$, and a combination of this plus a leading-edge slat can achieve $C_{L,\max} \approx 4.0$. These are not scientific curiosities; for instance, the Boeing 727 commercial jet aircraft uses a triple-slotted flap plus a leading-edge slat during landing.

Military airplanes are able briefly fly above the stall α via quick manevuers and some airplanes can even maintain flight while stalled, e.g., the Grumman X-29 experimetnal airplane set a record by maintaining flight at $\alpha = 67$ deg.

Fig. 7.28 Performance of airfoils with and without high-lift devices: A = NACA 0009; B = NACA 63-009; C = Kline–Fogleman airfoil; D to I shown in (a): (a) types of high-lift devices; (*Kline, Richard L. and Floyd F. Fogleman. "Airfoil for Aircraft." U. S. Patent 3706430, 1972.*) (b) lift coefficients for various devices; (*Spalding, D. B. "A Single Formula for the Law of the Wall." Journal of Applied Mechanics 28, no. 3 (September 1961): 455–458.*)